


Switching on Antiferromagnetic Coupled Superparamagnetism by Annealing Ferromagnetic Mn/CdS Nanoparticles

Balaji Sambandam,[†] Nallaiyan Rajendran,[†] Moorthi Kanagaraj,[§] Sonachalam Arumugam,[§] and Periakaruppan T. Manoharan^{*,†,||}

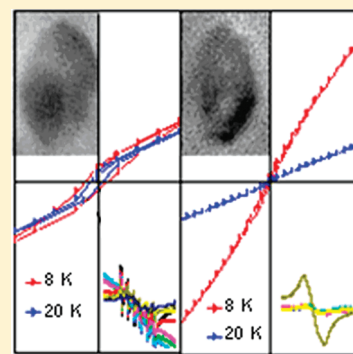
[†]Sophisticated Analytical Instruments Facility and Department of Chemistry, Indian Institute of Technology/Madras, Chennai 600 036, India

[‡]Department of Chemistry, Anna University, Chennai 600 025, India

[§]Centre for High Pressure Research, School of Physics, Bharathidasan University, Tiruchirappalli 620 024, India

 Supporting Information

ABSTRACT: Mixed phases of metastable cubic and stable hexagonal manganese assisted CdS nanoparticles were synthesized by a colloidal route. These phases were quantified by the Short and Steward method of X-ray diffraction and differential scanning calorimetry analysis. The photoluminescence (PL) emission observed around ~ 550 nm for undoped CdS is found to be due to cadmium vacancy defects; on increased addition of Mn^{2+} both the intensity and the line width of this emission continuously but disproportionately decrease and a new emission around ~ 585 nm, interpreted to be due to manganese d–d emission, emerges with increased intensity but with no change in line width. The disproportionate decrease in the area and bandwidth of the ~ 550 nm emission reveals that the intensity decrease is not a manifestation of the line width change. This decrease in intensity, i.e., the transition probability, is attributed to both the quenching effect by manganese and reduction in Cd vacancy defects due to substitution by Mn^{2+} . The enriched 5% Mn/CdS was subjected to annealing in order to find out any possible changes or transformation during the annealing process. An increase in the electron paramagnetic resonance intensity of preannealed sample on lowering temperature, much more than suggested by the Boltzmann population difference, indicates it to be ferromagnetic. On the other hand, postannealed sample exhibits antiferromagnetic coupled superparamagnetism as revealed by a drastic reduction in intensity down to the Néel temperature (T_N) with unaltered line width and a substantial decrease in line width below T_N . This conversion from ferromagnetism to antiferromagnetic coupled superparamagnetism after annealing is strongly supported by magnetic measurements, in which the preannealed sample exhibits increased coercivity on lowering the temperature, a case of ferromagnetism, and the postannealed material, however, exhibits low coercivity along with exchange bias below T_N , representing superparamagnetism. This conversion is due to ionic migration of Mn^{2+} as supported by magnetic and PL measurements. High-resolution transmission electron microscopy confirms the morphology and size of nanoparticles.



1. INTRODUCTION

The field of dilute magnetic semiconductors (DMSs) is an interesting area as the doping agent can modify or modulate the optical, magnetic, and structural behaviors.^{1,2} Introduction of even a small concentration of magnetic metal ion in DMS could play a crucial role by changing the host structure by either complete transformation³ or stepwise transformation^{4,5} as a function of its concentration. Complete transformation is possible in certain cases on the addition of a definite concentration of the magnetic or nonmagnetic ions.³ However, the latter stepwise transformation always leads to a mixture of two phases. The percentage of such mixed phases can be elucidated by methods such as powder X-ray diffraction through Debye function analysis (DFA),⁶ the Short and Steward method,⁷ simulation,⁸ and by differential scanning calorimetry (DSC).⁵ However, their physical properties depend on the percentage of phases, nature of the metal ion, and size and shape of the host matrix. An important tunable property is magnetism as part of a search for room

temperature ferromagnetism (FM), ferrimagnetism, superparamagnetism (SPM), or other complex magnetic behaviors because of their potential application for making of devices or just for pure theoretical/experimental interests. The resultant magnetic properties depend on synthetic methodologies, concentration, site occupation, clustering of ions, thermal treatment, physical state, size of quantum dots, or cluster, and shape of the host materials.^{9,10} The ferromagnetism is said to be caused by sp–d exchange interactions of the band carriers with localized magnetic ions.¹¹ By comparison, most of the II–VI DMSs show diverse magnetic phases, ranging from paramagnetism (PM), spin-glass-like antiferromagnetism (AFM), to ferromagnetism at low or very low temperature.¹² Only a few show ferromagnetism at room temperature.¹³ On the other hand, many examples of the

Received: February 23, 2011

Revised: May 12, 2011

Published: May 13, 2011

Mn/CdS are known to exhibit ferromagnetic properties around cryogenic temperatures.^{14,5} More often, manganese-doped CdS and CdSe have been reported to exhibit superparamagnetism¹⁵ or antiferromagnetism coupled superparamagnetism¹⁶ at low temperature.

We report here the magnetic properties observed in mixed phases of zinc blende and wurtzite structure of manganese-doped CdS nanoparticles which have been confirmed and quantified by both powder XRD (Short and Steward method⁷) and DSC measurements.⁵ Though the nanoparticles of 5 mol % Mn²⁺/CdS samples prepared in the medium of CTAB surfactant and propylene diamine (PD) ligand prior to annealing exhibits low temperature ferromagnetic behavior the same after annealing reveals antiferromagnetism with a Néel temperature (T_N) of 32 K, followed by superparamagnetism below this temperature due to uncompensated surface spins. This finding has been supported by electron paramagnetic resonance (EPR) measurements as it can reveal AFM and SPM nature at lower temperature through a measurement of temperature-dependent intensity and line width.

2. MATERIALS AND METHODS

2.1. Preparation of CTAB/PD Assisted CdS and Mn²⁺/CdS Nanoparticles. The chemicals used in our experiments, cetyl trimethylammonium bromide (Loba Chemie, 99.5%), propylenediamine (Alfa Aesar, 98%), cadmium nitrate tetrahydrate (Merck, 99%), manganese acetate tetrahydrate (Merck, 99.5%), and thiourea (Rankem, 99%), were used as purchased. Milli-Q Millipore ultrapure water was used for all reactions.

Three grams of CTAB was dissolved in very minimum amount of ultrapure distilled water. To this 0.308 g of cadmium nitrate and 10 mL of 1, 3-diaminopropane (propylenediamine, PD) were added and the resultant solution was kept for refluxing with constant stirring in nitrogen atmosphere. During the refluxing, 0.228 g of thiourea was added and the refluxing continued for a few hours at 120 °C. The appearance of a pale yellow precipitate indicates the formation CdS nanoparticles. The precipitate was washed with distilled water and methanol several times. Finally the product was thoroughly dried in the oven at 80 °C for 3 h. The same procedure was adopted for other preparations of 0.5, 1, and 5% with appropriate manganese and cadmium concentrations.

2.2. Measurement Details. A Bruker Discover D8 diffractometer with a Cu K α rotating anode source was used for X-ray powder diffraction analysis. The powdered Mn/CdS nanoparticles were placed in a glass plate and measured. The X-ray pattern was identified by comparison to phases in the powder diffraction file (PDF) database (ICDD, release 2000). DSC measurements have been done by using a DSC 204 Netzsch Thermal Analyzer. In order to quantify the percentages of the phases, we have done a systematic measurement with accurately weighed samples. All measurements were made under a nitrogen atmosphere with a heat flow rate of 5 °C/min. The magnetic susceptibility was measured using Quantum Design 9T PPMS with VSM and helium reliquifier magnetometer and Lakeshore VSM 7410. For making magnetic measurements, the sample was processed into a fine powder and vacuum sealed inside a quartz tube. The tube was then mounted in a straw for attachment to the sample probe. The temperature-dependent dc magnetization was measured using a zero-field-cooled (ZFC) protocol from 2 to 300 K in a measuring field of 100 Oe. The measurement was then repeated

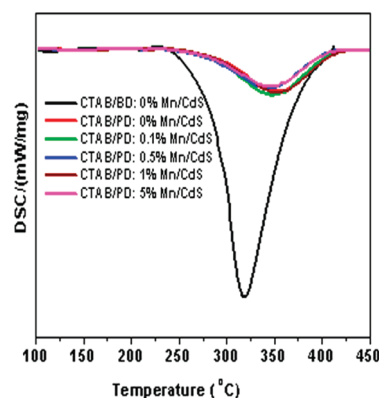


Figure 1. DSC profile for CTAB/BD without Mn²⁺ assisted CdS and CTAB/PD with and without Mn²⁺ assisted CdS nanoparticles.

over the same temperature range and measuring field using a field-cooled (FC) protocol in a cooling field of 100 Oe. The field-dependent dc magnetic susceptibility was measured over a range of +3 to −3 T at temperatures ranging from 8 to 300 K. The electron paramagnetic resonance (EPR) measurements were made by using a Bruker X-band continuous wave EPR both at room temperature (300 K) and at liquid nitrogen temperature (77 K) and also by a Bruker ELEXSYS 500 (Bruker BioSpin) down to 8 K. JEOL JEM 3010 operating at 300 kV was used for high-resolution TEM studies for sample imaging. Samples were dispersed in ethanol, and a drop of the resultant colloid was placed on a carbon-coated copper grid and allowed to dry at room temperature under ambient conditions. EDS patterns were recorded using the attached Philips CM12 TEM analyzer. The atomic percentages have been calculated using the software in the instrument, which takes into consideration all parameters for correct measurement.

3. RESULTS AND DISCUSSION

3.1. Identification of Phases before and after Annealing.

The percentage ratio of cubic to hexagonal phases has been elucidated by DSC measurement. Figure 1 depicts the quantitative comparison of the DSC curves for CTAB/BD/0% Mn-CdS and CTAB/PD assisted with and without manganese-doped CdS nanoparticles. Here PD and BD stand for propylenediamine and butylenediamine, respectively. Quantitative calculation of the cubic phase present in the mixed phases of CTAB/PD with and without manganese-assisted CdS nanoparticles is made possible by comparing them with 100% cubic nature of CTAB/BD/0% Mn-CdS⁵ as the base or standard. The measurements on all CTAB/PD/X% Mn-CdS ($X = 0-5$) samples were performed under the same conditions of CTAB/BD/0% Mn-CdS nanocrystals⁵ using the same quantity of samples in all experiments. In the case of CTAB/BD assisted 0% Mn-CdS, the cubic to hexagonal transition (phase conversion) is 100% due to the presence of only the cubic component prior to DSC measurement, a case of 100% conversion from cubic to hexagonal. On the other hand, all Mn²⁺-assisted CTAB/PD samples in their mixed phase conditions have a certain ratio of cubic and hexagonal phases before being subjected to DSC measurement; hence the exothermic peak arises only from the cubic component in the mixture. Thus by measuring the area of the curve, the exact percentages of cubic and hexagonal forms have been calculated.

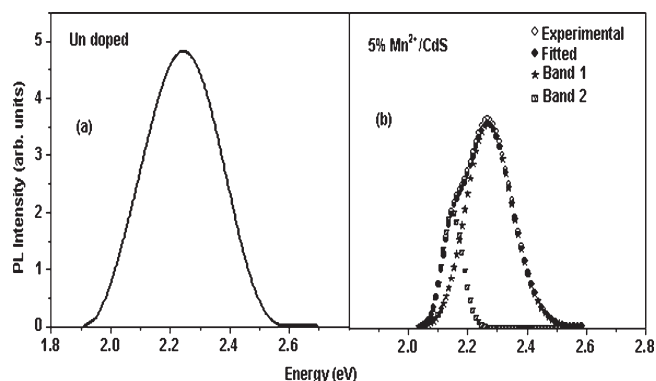


Figure 2. PL emission for (a) undoped and (b) 5% Mn^{2+} doped CdS nanoparticles.

The difference between the transition temperatures (differ in peak positions) of CTAB/BD/0% Mn-CdS sample and CTAB/PD/X% Mn/CdS based samples is attributed to increasing difficulty in solid state rearrangement, more so when one of the phases (metastable cubic phase) is present in a smaller concentration. Thus calculated values from DSC measurements are compared with the analysis by Short and Steward method of powder XRD data as shown in SI Table 1 in the Supporting Information. The XRD profiles for with and without manganese-doped CdS nanoparticles are depicted in SI Figure 1a in the Supporting Information along with those for the cubic phase of CTAB/BD/0% Mn-CdS in SI Figure 1b in the Supporting Information.

3.2. Photoluminescence of Preannealed and Postannealed Mn^{2+} /CdS Samples. Figure 2 depicts a typical PL emission spectrum of as-prepared undoped and 5% preannealed Mn^{2+} /CdS nanoparticles. Broad emission results in the region of 480–640 nm peaking at ~ 550 nm for undoped CdS; in addition to this broad (fwhm = 2667 cm^{-1}) band, a sharper but lower intensity emission in the region of 540–610 nm peaking at ~ 580 nm for manganese-doped CdS nanoparticles was observed when excited with 400 nm radiation. The broad major emission slightly shifts to 545 ± 2 nm initially but remains so on further addition up to 5% Mn^{2+} . But there is a substantial decrease in fwhm as a function of $[\text{Mn}^{2+}]$ from 2667 to 998 cm^{-1} (SI Table 2, Supporting Information) and so is the area under this emission curve. On the other hand though the intensity of the second emission at ~ 580 nm increases as a function of increasing $[\text{Mn}^{2+}]$; there is only a minor change in the line width from 805 to 831 cm^{-1} .

First of all, this single broad yellow-green emission (550 nm; 2.26 eV) irrespective of manganese addition is interpreted to be to cadmium-vacancy-related defect states, called V_{Cd} .¹⁷ The minor shift to lower λ_{max} on the addition of Mn^{2+} is due to either particle size reduction or increased band gap in presence of Mn^{2+} , the latter of which is in agreement with the optical measurement as shown in SI Figure 2 (Supporting Information). Second, the decreased ratio of intensity (5% Mn^{2+} vs undoped = 0.176) and that of the line width (0.374) substantially differ indicating that a faster reduction in area, i.e., corresponding oscillator strength or transition probability during the addition of Mn^{2+} , is not just a manifestation of reduction in the line width. This can be interpreted as follows: (i) A continuous decrease in the intensity of emission line (as monitored by area) while increasing the concentration of the manganese is not only due

to the quenching of the V_{Cd} by paramagnetic manganese ions through its spin–orbit effect but also due to reduction in the number of Cd vacancy sites by the occupation of Mn^{2+} . This type of quenching has been reported in many cases.^{17,18} (ii) But the slower line width reduction is attributed to the reduction in the number of cadmium vacancy intersite interactions specially when they are close to each other which in turn is actually responsible for the formation of exchange coupled dimers (vide infra) when occupied by manganese ions. Emissions from such intersite interactions are subjected to a kind of unresolved Davydov splitting¹⁹ and hence increased line width when present as dimer vacant sites; a single occupation of the same site will lead to decreased line width due to the loss of that splitting. The line width effect arises only from the loss of intersite interactions while the reduction in area comes from the two effects mentioned above. The presence of Cd vacancies is confirmed by an EDS profile as the atomic concentration of cadmium is found less than that of sulfur substantiating the V_{Cd} mechanism for the first emission (see Supporting Information).

On the other hand the orange emission at 580 nm (2.1 eV) is due to the well-established ${}^4\text{T}_1-{}^6\text{A}_1$ transition of the isolated Mn^{2+} ions (d–d emission). This emission intensity increases on increasing Mn^{2+} ion concentration as a result of more luminescent centers formed as can be related to EPR signal I with hyperfine lines (vide infra). It is important to note that this emission is normally observed around 570–590 nm, which can be easily seen in the deconvoluted emission profile CdS/ Mn^{2+} (panels a, b, and c of SI Figure 3a (Supporting Information) for 0.1, 0.5, and 1% Mn^{2+} /CdS, respectively, and Figure 2b). Though this emission is present even at low concentrations of Mn^{2+} , it is distinctly observable in concentration $\geq 1\%$ Mn/CdS. Furthermore, in contrast to the 550 nm emission with decreasing line width and disproportionate decrease in area, the line width of this d–d emission remains constant at around $820 \pm 10\text{ cm}^{-1}$ though the area under this curve increases, both on increasing $[\text{Mn}^{2+}]$, the latter of which reveals that this origin is purely of Mn^{2+} .

Another interesting comparison comes from the relative areas and hence intensities of this d–d emission in the preannealed and postannealed PL spectra of 5% Mn^{2+} /CdS samples, respectively, at 11960 and 5875 (SI Figure 3c,d (Supporting Information) and also SI Table 2 (Supporting Information)) indicating the migration of isolated Mn^{2+} ions to facilitate the formation of antiferromagnetically coupled dimers, in support of the magnetic data (vide infra).

As the Mn^{2+} d levels lie between the valence and conduction band regions of the CdS nanoparticles, they can readily capture the excited electrons from the band edge level as well as surface states.²⁰ An energy model proposed by Tanaka²¹ suggests that the energy transfer is most likely from the band edges of CdS (ZnS) or the recombination of carriers localized at Mn^{2+} ions. Thus the relative intensity of the orange and yellow-green emission depends on Mn^{2+} ion concentration and transition probabilities of the various steps involved in the band edge level.²¹ On the basis of the above statements a schematic diagram (SI Figure 4, Supporting Information) illustrates the energy process occurs in Mn^{2+} /CdS.

3.3. EPR Studies Predict Ferromagnetic (FM) Coupling in Preannealed and Antiferromagnetism Coupled with Superparamagnetism (AFM-SPM) in Postannealed 5% Mn^{2+} /CdS Samples. Figure 3 represents the variable temperature EPR spectra of CTAB/PD/5% Mn-CdS nanoparticles of preannealed

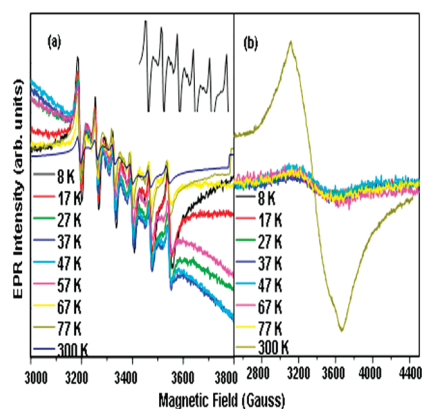


Figure 3. Variable-temperature EPR spectra of CTAB/PD assisted 5% manganese doped CdS nanoparticles (a) before (preannealed) (inset: magnified region of 10 forbidden lines flanked by 6 allowed lines) and (b) after annealing at 400 °C.

and postannealed samples at different temperatures from 300 to 8 K. A comparison of EPR spectra of CTAB/PD/0.1 to 5% Mn^{2+} /CdS nanoparticles at 300 and 77 K are shown in SI Figure 5 (Supporting Information). The manganese ions in preannealed samples feel two different environments as shown in Figure 3a; (i) signal I, six allowed hyperfine lines with 10 forbidden lines which are flanked by the allowed lines with an average hyperfine value of $A_{\text{iso}} = 6.9 \text{ mT}$ ($65.02 \times 10^{-4} \text{ cm}^{-1}$) characteristic of Mn^{2+} ion in a tetrahedral environment;¹⁹ (ii) signal II, a single broad line is due to formation of suggested Mn^{2+} – Mn^{2+} dimers with dipolar broadening and/or exchange coupling. The g value is approximately equal to 2. The overall EPR intensity of samples prior to annealing increases with decreasing temperature (77–8 K) as seen in SI Figure 6a (Supporting Information) suggesting low temperature ferromagnetism; also shown in SI Figure 7a (Supporting Information) are the EPR profile for three different temperatures. On the other hand, the postannealed sample shows a only a broad line at 300 K as seen in Figure 3b due to suggested Mn^{2+} – Mn^{2+} dimer/cluster formation which might be due to dipolar broadening and/or exchange coupling. It is of interest to note that the line width of the single line of the postannealed sample, i.e., broad signal II is higher (550 G) than that of preannealed (240 G) both measured at 300 K. This large difference, mainly due to dipolar mechanism, could have been caused by migration of Mn^{2+} ion during the annealing process leading to antiferromagnetism. The EPR intensity of postannealed sample decreases slowly with decrease in temperature and more drastically below 37 K as an indication of antiferromagnetic behavior of coupled manganese²² as shown in SI Figure 6b (Supporting Information). However, the continued observation of a lower intensity broad signal but with decreasing line width below this temperature can be attributed to superparamagnetism (SPM) due to disordered surface spins.²³ There is almost no change in the line width down to the Néel point. But we observe a sharpening of the signal, i.e., lowering of line width (ΔH_{pp}) slowly below the Néel temperature are 512, 460, and 360 G, respectively, at 27, 17, and 8 K as can be seen in SI Figure 7b (Supporting Information). While this sharpening is attributed to arise from fast spin relaxation on account of superparamagnetism,^{9,24} the reduced intensity below this Néel temperature (Figure 3b and SI Figure 6b (Supporting Information)) is due to antiferromagnetic impurity contribution.

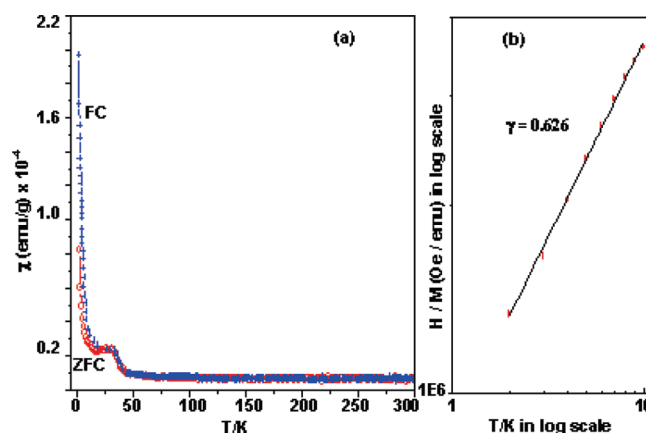


Figure 4. (a) ZFC (in red) and FC (in blue) curve for postannealed 5% Mn^{2+} /CdS nanoparticles. The T_N (Néel Temperature) is 32 K. (b) Typical log–log plot shows the fit of $H/M \propto T^{-\gamma}$ below 10 K. The line represents the fitting curve, whereas dots represent experimental values.

3.4. Magnetic Measurements Confirm the Predictions of EPR. The typical ZFC and FC measurements for postannealed CTAB/PD/5% Mn^{2+} /CdS sample are shown in Figure 4a. The inverse susceptibility indicates a Curie–Weiss temperature of $\Theta_p = -51 \text{ K}$ revealing the presence of antiferromagnetic coupling between the manganese atoms.²⁵ However, the increase in magnetization below the Néel temperature represents a new class of AFM and not like bulk antiferromagnetism where magnetization decreases below the Néel temperature.^{26–28} This increase in the low temperature magnetization (below T_N) generally depends on the particle size; larger magnetization results from smaller particle size.²⁹ Our observation of irreversibility between ZFC and FC below T_N is suggestive of superparamagnetism. Hence in this case T_N is not associated with T_B . Thus the magnetic behavior above the Néel temperature is antiferromagnetic, and below the T_N it represents SPM coupled with AFM. Some earlier reports indicate a decrease in the size of the MnS particles being associated with lowering of their T_N value³⁰ which in turn can cause higher Θ_p , for example, the Θ_p value for 80 nm MnS nanoparticles is higher (-174 K)^{30a} than that for bulk MnS (-490 K)^{30a,31} corresponding respectively to their T_N values, 116 and 130 K. These results imply that the magnetic properties are strongly dependent on their size and dimension. Our postannealed samples have a T_N value of 32 K with the corresponding $\Theta_p = -51 \text{ K}$, having a particle size of 5–15 nm. Though the former two values are from pure MnS and our observation is on diluted MnS in CdS, there seems to be some correlation between particle size, T_N , and Θ_p .

This behavior below T_N is suggested to originate from superparamagnetism coupled with antiferromagnetism^{26,27,29,32} as can be explained by either one of the two models: (i) a core–shell model in which a ferro/ferrimagnetic core with uncompensated spins on the surface (shell);³³ (ii) yet another core–shell model proposed by Bhowmik et al.²⁹ in which antiferromagnetic core with unbalanced (frustrated) surface shell. However, both antiferromagnetic and ferromagnetic systems can display superparamagnetism when the grain size is reduced to nanoscale level because of the possibility for excess uncompensated spins resulting from a larger surface.³⁴ From the above arguments, the nature of the core for our postannealed sample is antiferromagnetic as it goes parallel to the experimental observation of

reduction in EPR intensity on lowering temperature. To confirm our explanation by the core–shell model of Bhowmik et al.,²⁹ the result from a Curie type equation: $H/M = C/T^\gamma$, is shown as a log–log plot of H/M vs T in Figure 4b. A straight line for H/M vs T^γ behavior below 10 K depicts the presence of nanoparticles which are superparamagnetic in nature. A γ value of 1 represents a typical value for paramagnetic or superparamagnetic material. Thus the exponent γ value 0.626 (less than 1) indicates that the antiferromagnetic order of the core affects the superparamagnetic behavior of the shell.²⁶ The calculated exponent value of 0.626 for our postannealed sample is definitely higher than that for such other reported superparamagnetic systems, viz., CoRh_2O_4 ²⁹ and Cr_2O_3 .²⁶ In general, a higher particle size in these latter materials is found to be related to decreasing γ values. The γ value of 0.626 for our system is much higher than those for CoRh_2O_4 ²⁹ and Cr_2O_3 ,²⁶ having particle sizes of 16–70 nm ($\gamma = 0.49$ –0.23) and 20–40 nm ($\gamma = 0.31$ –0.16), respectively; this is in accordance with our observed smaller particle size of 5–15 nm. While the materials investigated by Bhowmik et al.²⁹ are pure magnetic in nature, ours constitute the diluted magnetism from DMS. Our suggestion of small particle size for the postannealed 5% $\text{Mn}^{2+}/\text{CdS}$ is strongly supported by the results from transmission electron microscopy (TEM).

The nature of uncompensated surface spins being affected by the core antiferromagnetism has been explained by Bhowmik et al.²⁹ The number of uncompensated spins depends upon the imbalance in exchange interactions on the shell which creates some preferential orientations to the shell spins, contributing to surface anisotropy field. When particle size decreases, this magnitude of anisotropy field increases; the contribution from the antiferromagnetic core is decreased which creates uncompensated (frustration) spins on the surface which are loosely bound to the core spins and hence pave the way to superparamagnetic behavior. A similar mechanism is proposed for our postannealed 5% $\text{Mn}^{2+}/\text{CdS}$ with surface uncompensated spins. In our case, frustrated spin formation possibly results from clusters with intermanganese interaction having, say, three Mn^{2+} ions, where two ions may represent the strongly coupled antiferromagnetic core with extra weakly bound Mn^{2+} protruding onto the surface as surface spin leading to SPM. This strong and weak coupling will create exchange imbalance.

The AFM behavior above T_N and AFM coupled/influenced SPM behavior below T_N are further supported by magnetization measurement. Figure 5 depicts M vs H curve above and below T_N . At 8 K, below T_N , as expected, there is a hysteresis loop with a measured coercivity of H_C : 755 Oe and remanence of H_R : 9.53×10^{-4} emu. Magana et al.⁹ reported SPM behavior in Mn/CdSe quantum dots below the blocking temperature ($T_B \sim 40$ K) with the measured coercive field of 0.1 T at 2 K followed by reduction in coercive field on increasing the temperature. In a similar fashion our system shows reduction in coercive field on increasing temperature of the sample suggesting the SPM behavior up to the transition point (T_N). The measured H_C and H_R at 20 K are 530 Oe and 1.71×10^{-4} emu, respectively, as shown in the inset of Figure 5a. However, there is a small deviation from the symmetry curve due to a small “exchange bias” toward negative field. The amount of exchange bias can be calculated from the equation of $H_{EB} = -(H_{C1} + H_{C2})/2$, where H_{C1} and H_{C2} are respectively of right and left coercive fields of the hysteresis loop.³⁵ From this equation, the measured H_{EB} values for both 20 and 8 K are 71 and 150 Oe, respectively. This again confirms the interparticle interaction in the system leading to subtle shifts

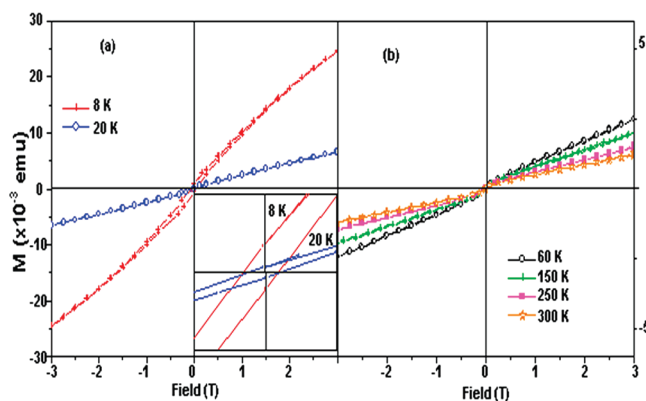


Figure 5. (a) M vs H curves for postannealed 5% $\text{Mn}^{2+}/\text{CdS}$ nanoparticles below T_N . (inset) Magnified region at 8 and 20 K. (b) M vs H curves above T_N .

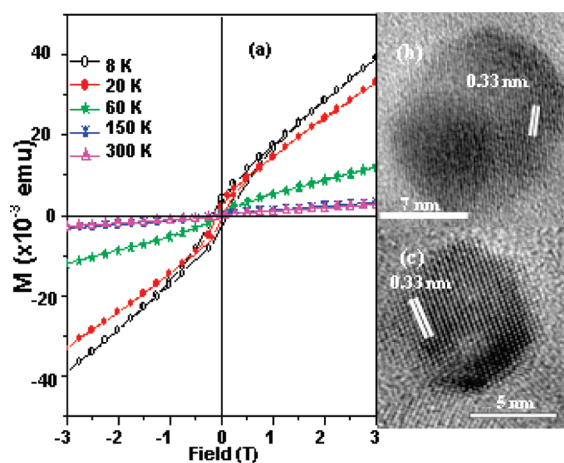


Figure 6. (a) M vs H curve for 5% $\text{Mn}^{2+}/\text{CdS}$ nanoparticles prior to annealing at various temperatures. (b) HRTEM image of 5% $\text{Mn}^{2+}/\text{CdS}$ nanoparticles prior to annealing and (c) the same for postannealed sample.

from the center of the M vs H curve. No magnetic saturation was detected down to ± 3 T. The observations of the hysteresis loop with low coercive field and exchange bias effect indicate existence of strong interparticle interactions, characteristics of AFM nanoparticles with SPM behavior.²⁶ It is noteworthy that H_{EB} decreases from very low temperature (8 K) to Néel temperature ($T_N \sim 32$ K); however, above T_N there is no exchange bias and no coercive field (Figure 5b). On the other hand, the preannealed sample exhibits good ferromagnetic behavior with measurable H_C (1508, 789, 650 Oe) and H_R (4.08, 2.26, 0.82×10^{-4} emu) at 8, 20, and 60 K, respectively, as represented in Figure 6a. All the above observations originate purely from MnS clusters and not from any other contamination of oxygen or other elements as supported by EDS analysis of postannealed sample as shown in SI Figure 8 (Supporting Information). The exchange interactions, in general, are distance dependent; long distances between interacting ions will lead to simple paramagnetism with no exchange, a decrease of distances between the free spins of Mn^{2+} ions with or without the intervention of diamagnetic cadmium ions will lead to FM. Even further decrease in the distance could result in AFM.³⁶ So the migration of Mn^{2+} ions

toward each other can become significant³⁷ during the annealing process, causing the transformation from FM (prior to annealing) to AFM + SPM (postannealing).

3.5. HRTEM Measurements. The HRTEM images for single particles of pre- and postannealed samples of 5% Mn²⁺/CdS are shown in panels b and c of Figure 6, respectively, with well-known measured *d* values (two more images are shown in the Supporting Information, SI Figure 9a and 9b of pre- and postannealed samples, respectively). We cannot easily distinguish the phases from transmission electron microscopy as the cubic (111) and hexagonal (002) planes share the same lattice spacing of 0.33 nm in preannealed sample (Figure 6b and SI Figure 9a, Supporting Information). Variation of particle sizes from 6 to 15 nm indicates a lack of uniformity in their sizes. However, the postannealed sample shows clear lattice fringes (column of atoms) with measured *d* value of 0.33 nm confirming its uniform hexagonal (002) plane. This is further supported by the XRD of the annealed sample as shown in SI Figure 1c (Supporting Information).

4. CONCLUSION

In conclusion, mixed phases of zinc blende and wurtzite have been identified in CTAB/PD/X% Mn/CdS and quantified by their XRD and DSC profiles. The PL emission properties have shown the presence of two bands, one at ~550 nm and the other at ~580 nm, the former being due to defect emission and the latter due to manganese d–d emission. The preannealed sample of 5% manganese-doped CdS exhibits ferromagnetism (FM) whereas the postannealed sample shows AFM coupled SPM behavior below the Néel temperature. Support for both behaviors comes from temperature-dependent EPR intensity measurements where the former depicts intensity enhancement and latter showed reduction on decreasing the temperature down to 8 K. Further confirmation is derived from magnetism and XRD. Ferromagnetism of preannealed samples changes to AFM+SPM after the annealing process, and this change is attributed to ionic migration during annealing.

■ ASSOCIATED CONTENT

Supporting Information. Percentages of cubic and hexagonal phases calculated from XRD and DSC, XRD for preannealed and postannealed samples; PL emissions; EPR at 300 and 77 K for preannealed samples; temperature-dependent EPR intensity profiles for pre- and postannealed 5% Mn²⁺/CdS samples, comparison of EPR profiles at three different temperatures, EDS for undoped and postannealed 5% Mn²⁺/CdS samples, and HRTEM images for pre- and postannealed samples. This material is available free of charge via the Internet at <http://pubs.acs.org>.

■ AUTHOR INFORMATION

Corresponding Author

*E-mail: ptm@iitm.ac.in.

Notes

[†]Sir C.V. Raman Chair Professor, IGNOU, New Delhi.

■ ACKNOWLEDGMENT

P.T.M. acknowledges the DST, Government of India for research scheme (SR/S1/RFIC-02/2006) and for the Ramanna

Fellowship. He also thanks the IGNOU, Delhi for the Sir C.V. Raman Chair Professorship. Balaji thanks the CSIR for his Senior Research Fellowship (09/468(0412)/2009-EMR-1). We thank Professor J. Subramanian of CLRI and Dr. J. M. Rifkind and Dr. Maria Selgado of NIA/NIH, Baltimore for help in low temperature EPR measurements. S.A. and M.K. wish to acknowledge DST and UGC, New Delhi for the financial support.

■ REFERENCES

- (1) Norberg, N. S.; Kittilstved, K. V.; Amonette, J. E.; Kukkadapu, R. K.; Schwartz, D. A.; Gamelin, D. R. *J. Am. Chem. Soc.* **2004**, *126*, 9387.
- (2) Sooklal, K.; Cullum, B. S.; Angle, S. M.; Murphy, C. J. *J. Phys. Chem.* **1996**, *100*, 4551.
- (3) Patil, L. A.; Weni, P. A.; Amalnerkar, D. A. *Mater. Chem. Phys.* **1999**, *61*, 260.
- (4) Biswas, S.; Kar, S.; Chaudhuri, S. *J. Phys. Chem. B* **2005**, *109*, 17526.
- (5) Sambandam, B.; Jude Vimal Michael, R.; Rajendran, N.; Arumugam, S.; Manoharan, P. T. Unpublished work.
- (6) Vogel, W.; Urban, J.; Kundu, M.; Kulkarni, S. K. *Langmuir* **1997**, *13*, 827.
- (7) Short, M. A.; Steward, E. G. *Am. Mineral.* **1959**, *44*, 189.
- (8) Marandi, M.; Taghavinia, N.; Sedaghat, Z.; Irajizad, A.; Mahdavi, S. M. *Nanotechnology* **2008**, *19*, 225705.
- (9) Magana, D.; Perera, S. C.; Harter, A. G.; Dalal, N. S.; Strouse, G. F. *J. Am. Chem. Soc.* **2006**, *128*, 2931.
- (10) (a) Gamelin, D. R. Doped Semiconductor nanocrystals: Synthesis, Characterization, Physical Properties and Applications. In *Progress in Inorganic Chemistry*; D., K. K., Ed.; John Wiley: Hoboken, NJ, 2005; Vol. 54. (b) Norman, T. J., Jr.; Magana, D.; Wilson, T.; Burns, C.; Zhang, J. Z.; Cao, D.; Bridges, F. *J. Phys. Chem. B* **2003**, *107*, 6309. (c) Feltin, N.; Levy, L.; Ingert, D.; Pileni, M. P. *J. Phys. Chem. B* **1999**, *103*, 4.
- (11) Diet, T.; Ohno, H.; Mastsukura, F.; Ciebert, J.; Ferrand, D. *Science* **2000**, *287*, 1019.
- (12) Saito, H.; Zates, W.; Yamagata, S.; Suauki, Y.; Ando, K. *J. Appl. Phys.* **2002**, *91*, 8085.
- (13) (a) Delikanli, S.; He, S.; Qin, Y.; Zhang, P.; Zeng, H. *Appl. Phys. Lett.* **2008**, *93*, 132501. (b) Bhattacharyya, S.; Estrin, Y.; Rich, D. H.; Zitoun, D.; Koltypin, Y.; Gedanken, A. *J. Phys. Chem. C* **2010**, *114*, 22002.
- (14) Kim, D. H.; Lee, D. J.; Kim, N. M.; Lee, S. J.; Kanga, T. W.; Woo, Y. D.; Fu, D. J. *J. Appl. Phys.* **2007**, *101*, 094111.
- (15) Chen, C. C.; Hsu, Y. J.; Lin, Y.-F.; Lu, S. -Y. *J. Phys. Chem. C* **2008**, *112*, 17964.
- (16) Bhattacharyya, S.; Zitoun, D.; Gedanken, A. *J. Phys. Chem. C* **2008**, *112*, 7624.
- (17) Wang, Y.; Herron, N. *J. Phys. Chem.* **1988**, *92*, 4988.
- (18) Biswas, S.; Kar, S.; Chaudhuri, S. *J. Phys. Chem. B* **2005**, *109*, 17526.
- (19) Sambandam, B.; Manoharan, P. T. *J. Phys. Chem. C* **2009**, *113*, 9486.
- (20) Sapra, S.; Prakash, A.; Ghanghrekhar, A.; Periasamy, N.; Sarma, D. D. *J. Phys. Chem. B* **2005**, *109*, 1663.
- (21) Tanaka, M. *J. Lumin.* **2002**, *100*, 163.
- (22) (a) Feltin, N.; Levy, L.; Ingert, D.; Vincent, E.; Pileni, M. P. *J. Appl. Phys.* **2000**, *87*, 1415. (b) Heinrich, B. K.; Ossau, W.; Litz, T.; Waag, A.; Landwehr, G. *J. Appl. Phys.* **1994**, *75*, 8046.
- (23) Tobia, D.; Winkler, E. L.; Zysler, R. D.; Granada, M.; Troiani, H. E. *J. Alloys Compd.* **2010**, *495*, 520.
- (24) (a) Sharma, V. K.; Waldner, F. *J. Appl. Phys.* **1977**, *48*, 4298. (b) Tronconi, A. L.; Morais, P. C.; Peglerini, F.; Tourinho, F. A. *J. Magn. Mater.* **1993**, *122*, 90.
- (25) Kim, D. S.; Lee, J. Y.; Na, C. W.; Yoon, S. W.; Kim, S. Y.; Park, J.; Jo, Y.; Jung, M. -H. *J. Phys. Chem. B* **2006**, *110*, 18262.
- (26) Bhowmik, R. N.; Ranganathan, R. *Solid State Commun.* **2007**, *141*, 365.

- (27) Punnoose, A.; Magnone, H.; Seehra, M. S.; Bonevich, J. *Phys. Rev. B* **2001**, *64*, 174420.
- (28) -Vazquez, C. V.; -Lopez, M. B.; -Quintela, M. A.; Hueso, L. E.; Rivas, J. J. *J. Magn. Magn. Mater.* **2004**, *272–276*, 1547.
- (29) Bhowmik, R. N.; Nagarajan, R.; Ranganathan, R. *Phys. Rev. B* **2004**, *69*, 054430.
- (30) (a) Kan, S.; Felner, I.; Banin, U. *Isr. J. Chem.* **2001**, *41*, 55.
(b) Jun, Y.; Jung, Y.; Cheon, J. *J. Am. Chem. Soc.* **2002**, *124*, 615.
- (31) Banewicz, J. J.; Lindsay, R. *Phys. Rev.* **1956**, *104*, 318.
- (32) Trohidoua, K. N.; Zianni, X.; Blackman, J. A. *J. Appl. Phys.* **1998**, *84*, 2795.
- (33) Chen, J. P.; Sorensen, C. M.; Klabunde, K. J.; Hadjipanayis, G. C. *Phys. Rev. B* **1995**, *51*, 11527.
- (34) Néel, L. *Ann. Geophys.* **1949**, *5*, 99.
- (35) Tian, Z. M.; Yuan, S. L.; Liu, L.; Yin, S. Y.; Jia, L. C.; Li, P.; Huo, S. X.; Li, J. Q. *J. Phys. D: Appl. Phys.* **2009**, *42*, 035008.
- (36) Panse, C.; Leitsmann, R.; Bechstedt, F. *Phys. Rev. B* **2010**, *82*, 125205.
- (37) (a) Bruno, P.; Chappert, C. *Phys. Rev. B* **1992**, *46*, 261.
(b) Richardson, H. W.; Hatfield, W. E. *J. Am. Chem. Soc.* **1976**, *98*, 835.